Journal of Applied Analysis and Computation
Volume 16, Number 4, August 2026, 1736–1755
Website:http://www.jaac-online.com
DOI:10.11948/20250286

ANALYTICAL EIGENFUNCTION EXPANSION FOR TEMPERED TIME-FRACTIONAL ADVECTION DIFFUSION IN BOUNDED DOMAINS

Shankar Pariyar[1,3], Bishnu P. Lamichhane[2], Jeevan Kafle[3,†] and Eeshwar Prasad Poudel[1,3]

Abstract This work develops an analytical–computational approach for solving the tempered time-fractional advection–diffusion equation on a rectangular domain with homogeneous Dirichlet boundary conditions. The model, based on the Caputo tempered fractional derivative, captures anomalous transport, transitioning from nonlocal, memory–driven subdiffusion to standard diffusion. A closed–form series solution is obtained by combining an eigenfunction expansion of sine spatial modes with a Laplace transform in time, in which the temporal dynamics are governed by tempered Mittag–Leffler kernels. The solution demonstrates consistency with established models: As the fractional order $\alpha \to 1$, it converges to the classical diffusion equation with an effective sink. When the tempering parameter $\theta = 0$, it reduces to the standard Caputo formulation. The framework efficiently transforms the original boundary-value problem into a sum of quickly converging modes, thereby enabling accurate numerical calculations using a limited number of terms from the eigenfunction expansion. Theoretical and numerical analyses, including surface plots and error tables, confirm the convergence and high accuracy of the method. Parametric analysis shows that the fractional order α mainly controls the memory effects and spatial spread characteristics of subdiffusion, whereas the tempering parameter θ introduces an exponential truncation that accelerates temporal decay. The effectiveness of the method is illustrated through a street canyon application, where pollutant build-up, delayed dispersion, and subsequent clearance under limited ventilation are captured. This study not only underscores the framework's relevance for urban air quality modeling but also establishes it as a valuable benchmark for validating numerical solvers and reduced-order models.

Keywords Time-fractional advection–diffusion, tempered fractional derivative, eigenfunction expansion, Mittag–Leffler kernel, pollutant dispersion, urban air-quality modeling.

MSC(2010) 35R11, 35C10, 76R50, 76M25.

1. Introduction

Classical advection-diffusion models employing integer-order derivatives have been conventionally utilized to characterize the movement and dispersion of substances [20, 34]. These models

[†]The corresponding author.
[1]Department of Mathematics, Tri-Chandra Multiple Campus, Tribhuvan University, Ghantaghar, Kathmandu, Nepal
[2]School of Information and Physical Sciences, University of Newcastle, Australia
[3]Central Department of Mathematics, Tribhuvan University, Kirtipur, Kathmandu, Nepal
Email: shankar.pariyar@trc.tu.edu.np(S. Pariyar), bishnu.lamichhane@newcastle.edu.au(B. P. Lamichhane), jeevan.kafle@cdmath.tu.edu.np(J. Kafle), eeshwarpoudel475@gmail.com(E. P. Poudel)

generally produce Gaussian-shaped plumes and demonstrate exponential decay toward equilibrium [43]. Nonetheless, numerous physical and environmental systems exhibit substantial deviations from this idealized behavior [16,17]. Such anomalies are observed in instances like solute transport in aquifers, pollutant dispersion in heterogeneous terrains, and chemical exchange in confined reactors [1, 29]. In these contexts, particle dispersion displays anomalous behavior, where the mean squared displacement grows nonlinearly-either more slowly in subdiffusion or more rapidly in superdiffusion-deviating from the linear scaling characteristic of Brownian motion [37,38]. These phenomena are well documented across studies in porous media, hydrological systems, and atmospheric dispersion [3,33]. Consequently, there is a clear need for mathematical frameworks capable of accurately modeling such non-Fickian dynamics [36]. This widespread evidence of anomalous transport challenges the predictive power of classical integer-order models and motivates more advanced mathematical tools [18].

The observed anomalous transport behaviors underscore the limitations inherent in classical advection-diffusion models, thereby necessitating the development of more comprehensive mathematical frameworks [8, 42]. In this context, fractional calculus offers a robust and adaptable methodology for representing complex dynamical processes that traditional models fail to adequately capture [36]. The tempered fractional derivative represents an extension of the classical fractional derivative, achieved by incorporating an exponential factor into the kernel [2, 23]. A tempering parameter, denoted as θ, regulates the rate at which this exponential term mitigates the influence of long memory; setting $\theta = 0$ reverts to the classical Caputo fractional derivative operator. Temporal derivatives of non-integer order effectively encapsulate memory effects and heavy-tailed waiting-time distributions, while spatial fractional operators characterize nonlocal transport mechanisms, such as Lévy flights [23, 25, 37, 38]. The theoretical underpinnings and practical applications of these models have been extensively developed within the fields of physics and engineering [31]. However, purely fractional formulations may predict unbounded variances and excessively heavy tails over extended periods, which are inconsistent with physical reality. Recent studies have further demonstrated that anomalous diffusion in bounded or confined domains may exhibit persistent nonergodic behavior, even in the presence of restoring forces or confinement, depending on the underlying memory mechanisms and boundary conditions [10]. In particular, Liang et al. (2023) investigated the nonergodic behavior of confined fractional Brownian motion, showing pronounced ergodicity breaking in the superdiffusive regime [21]. In such anomalous diffusion systems, stochastic resetting has been shown to act as an effective confining mechanism that strongly influences relaxation, stationary states, and ergodic properties—potentially inducing ergodicity breaking or, under particular constraints on the resetting-time distribution, enabling the re-emergence of ergodic behavior [39]. Tempered fractional operators address this limitation: The exponential cutoff maintains anomalous transport for short and intermediate durations while ensuring bounded variance and realistic decay asymptotically [24, 27].

Efficient numerical methods for time fractional diffusion equations (TFDEs) are crucial for accurately modeling finite-memory processes in science and engineering. Extensive research has been dedicated to developing high-order methods for solving space–fractional equations. Pariyar et al. [29] proposed a one-dimensional time-fractional model for the dispersion of NH_3, CO, and CO_2, although it was unable to capture complex urban topography. Classical stochastic frameworks, including the Ornstein–Uhlenbeck process, are commonly employed in diffusion modeling because of their analytical simplicity. Nevertheless, Cherstvy et al. (2018) [10] demonstrated that despite exhibiting short-lived non-ergodic effects under nonequilibrium initial conditions, the inherently Markovian structure of the Ornstein–Uhlenbeck process confines

temporal correlations, limiting its ability to capture long-memory dynamics typical of transport and environmental systems. Zhao et al. [43] introduced a fourth-order ADI algorithm specifically designed for the two-dimensional nonlinear space–fractional Schrödinger equation. Liu et al. [22] developed an ADI finite-difference framework for simulating the fractional FitzHugh–Nagumo monodomain system in two dimensions. Concurrently, Zayernouri and Karniadakis [41] proposed several classes of high-order strategies for fractional partial differential equations. Building on spectral techniques, Bhrawy and Zaky [6] devised a high-order method for variable-order space–time fractional Schrödinger problems, while Bhrawy et al. [4] advanced the Q-SLT scheme for systems involving multi-order fractional derivatives. Various advanced methods have been proposed for fractional PDEs, including Q-SLT and Jacobi tau schemes [4,5,7], generating functions for Riesz derivatives [14], operational matrices [32], element-free Galerkin techniques [11], and high-order algorithms for Riesz operators [13]. Sultana et al. [35] conducted a comparative study of linear, quadratic, and quadratic-linear finite-difference schemes for tempered fractional integro-differential equations. Despite the existence of several numerical approaches for tempered fractional integro-differential equations, the analytical treatment of tempered time-fractional advection–diffusion equations in bounded domains has received limited attention [12]. Although various numerical schemes have been proposed for tempered fractional advection–diffusion equations, analytical eigenfunction expansions in two-dimensional bounded domains remain underdeveloped.

This study contributes by establishing an exact sine-series representation under the tempered Caputo framework, which distinctly separates spatial structure from temporal memory effects. To establish such a framework, it is essential to recall the underlying operators that govern these models. The Caputo derivative of order $\alpha \in (0,1)$ encapsulates power-law waiting times and long-range temporal correlations. Nevertheless, purely fractional models may exhibit unrealistically heavy tails at later times. Tempering addresses this issue by exponentially truncating the memory kernel while preserving the desired anomalous behavior at short and intermediate times. This results in the tempered time-fractional Advection–Diffusion equation

$$ {}^{C}D_t^{\alpha,\theta}\, C(x,y,t) \;=\; D\,(C_{xx}+C_{yy}) - u_x\,C_x - u_y\,C_y, \qquad (x,y)\in\Omega,\ t>0, \tag{1.1}$$

posed on a bounded domain with diffusion coefficient $D>0$, advective field (u_x,u_y), fractional order $\alpha\in(0,1]$, and tempering parameter $\theta\geq 0$ and the operator ${}^{C}D_t^{\alpha,\theta}C(x,y,t)$ is defined in ref. (2.3). When $\theta=0$, equation (1.1) simplifies to the standard Caputo model. As $\alpha\to 1$, the equation converges to the classical advection–diffusion equation, which is augmented by a linear sink term $-\theta C$. Bounded domains with homogeneous Dirichlet boundary conditions are representative of fully absorbing walls and serve as prototypical models for street canyons, laboratory channels, and valley-like compartments [9, 29]. In these geometries, eigenfunction methods offer solutions that are physically transparent, effectively separating spatial structure from temporal attenuation. Despite their advantages, closed-form eigenfunction expansions for the tempered Caputo case—particularly in two spatial dimensions with advection—remain relatively underdeveloped. Existing analyses often address untempered fractional diffusion, focus on unbounded or one-dimensional settings, or depend on purely numerical discretizations that obscure the interactions between α, θ, and the geometry [31, 42].

This work develops an analytical eigenfunction framework for solving equation (1.1) on a rectangular domain with homogeneous Dirichlet boundary conditions. Our approach combines separation of variables with Laplace transforms in time, yielding a convergent series representation in which spatial modes are sine functions and whose modal amplitudes evolve according to

tempered Mittag–Leffler functions. The resulting formulas expose how α controls subdiffusive spreading and memory-driven retention, while θ introduces an exponential cutoff that accelerates clearance without altering spatial shapes determined by the boundary-value problem. We derive a sine-sine series solution for $C(x, y, t)$, where each mode evolves as $\mathrm{e}^{-\theta t} E_{\alpha,1}(-\lambda_{nm} t^{\alpha})$ with λ_{nm} denoting the Laplacian eigenvalues. For constant wind components (u_x, u_y), the advection term vanishes under projection, onto the eigenfunctions, thereby isolating the effects of diffusion, fractional order, and tempering. Explicit Coefficient formulas project arbitrary initial condition $f(x, y)$ onto the eigenbasis, ensuring reproducibility and straightforward implementation. The model reduces to the standard Caputo case when $\theta = 0$, recovers classical diffusion with a sink term as $\alpha \to 1$, and is consistent with the asymptotic behavior of the tempered Mittag–Leffler function. By separating spatial geometry from temporal memory, the framework clarifies parameter roles and supports calibration and analysis. Standard fractional models reproduce slow power-law relaxation but can exaggerate persistence at large t. The exponential tempering factor $\mathrm{e}^{-\theta t}$ retains subdiffusive behavior at early times while enforcing realistic decay at longer scales, balancing memory-driven transport with finite residence times—a key feature in bounded or semi-enclosed domains.

The paper is structured as follows. Section 2 introduces the problem setup and the tempered Caputo operator. Section 3 develops the eigenfunction expansion and derives modal solutions. Section 4 verifies consistency and limiting cases. Section 5 presents analytical results and discusses the influence of parameters. Section 6 applies the framework to urban street-canyon pollutant dispersion. Finally, Section 7 concludes with key findings and possible extensions.

2. Fundamentals of fractional calculus

Let f be a sufficiently regular function defined on the finite interval $[0, T]$. Let $\alpha > 0$ denote the fractional order and $\theta \geq 0$ the tempering parameter. The tempered fractional operators generalize the classical Riemann–Liouville definitions by introducing an exponential decay factor that limits long-memory effects.

Definition 2.1. ([19]) Tempered Riemann–Liouville fractional integral. The tempered fractional integral of order α is defined as

$$(I_t^{\alpha,\theta} f)(t) = \frac{1}{\Gamma(\alpha)} \int_0^t e^{-\theta(t-\tau)} (t-\tau)^{\alpha-1} f(\tau)\, d\tau, \qquad t \in [0, T]. \tag{2.1}$$

When $\theta = 0$, this reduces to the standard Riemann–Liouville fractional integral:

$$(I_t^{\alpha,0} f)(t) = \frac{1}{\Gamma(\alpha)} \int_0^t (t-\tau)^{\alpha-1} f(\tau)\, d\tau.$$

Definition 2.2. ([40]) Tempered Riemann–Liouville fractional derivative. For $n - 1 < \alpha < n$ and $n \in \mathbb{N}$, the corresponding tempered fractional derivative is given by

$$(D_t^{\alpha,\theta} f)(t) = e^{-\theta t} \frac{d^n}{dt^n} \left[\frac{1}{\Gamma(n-\alpha)} \int_0^t e^{\theta\tau} (t-\tau)^{n-\alpha-1} f(\tau)\, d\tau \right]. \tag{2.2}$$

When $\theta = 0$, Eq. (2.2) becomes the classical Riemann–Liouville fractional derivative:

$$(D_t^{\alpha,0} f)(t) = \frac{d^n}{dt^n} \left[\frac{1}{\Gamma(n-\alpha)} \int_0^t (t-\tau)^{n-\alpha-1} f(\tau)\, d\tau \right].$$

Table 1. Description of parameters.

Parameter	Description
$C(x, y, t)$	Pollutant concentration field
$f(x, y)$	Initial concentration distribution at $t = 0$
t	Time [s]
(x, y)	Spatial coordinates [m]
$\Omega = [0, L_x] \times [0, L_y]$	Rectangular spatial domain
$L_x,\ L_y$	Domain lengths in x and y [m]
D	Molecular/eddy diffusion coefficient [m^2/s]
$u_x,\ u_y$	Constant advective velocities [m/s]
α	Fractional order of the time derivative, $0 < \alpha \leq 1$
θ	Tempering parameter (exponential cutoff rate) [s^{-1}]
${}^{C}D_t^{\alpha,\theta}$	Tempered Caputo fractional derivative in time
$E_{\alpha,\beta}(z)$	Two-parameter Mittag–Leffler function
$\phi_n(x) = \sin\left(\frac{n\pi x}{L_x}\right)$	Sine eigenfunction in x
$\psi_m(y) = \sin\left(\frac{m\pi y}{L_y}\right)$	Sine eigenfunction in y
$\lambda_n^{(x)},\ \lambda_m^{(y)}$	1D Laplacian eigenvalues
$\lambda_{n,m} = D\left(\lambda_n^{(x)} + \lambda_m^{(y)}\right)$	2D modal decay rate
$T_{n,m}(t)$	Temporal modal amplitude for mode (n, m)
$A_{n,m}$	Projection coefficient of $f(x, y)$ onto $\phi_n\psi_m$
$\mathcal{L}\{\cdot\}$	Laplace transform in time
BCs	Homogeneous Dirichlet boundaries, $C = 0$ on $\partial\Omega$ (absorbing)

Definition 2.3. ([19]) Tempered Caputo fractional derivative on $[0, T]$. For $n - 1 < \alpha < n$ and $n \in \mathbb{N}$, the left-sided Caputo tempered fractional derivative of order α is defined as

$$({}^{C}D_t^{\alpha,\theta} f)(t) = e^{-\theta t} \frac{1}{\Gamma(n-\alpha)} \int_0^t e^{\theta\tau} (t-\tau)^{n-\alpha-1} \frac{d^n f(\tau)}{d\tau^n}\, d\tau, \qquad t \in [0, T]. \tag{2.3}$$

When the tempering parameter $\theta = 0$, the above expression reduces to the classical Caputo fractional derivative:

$$({}^{C}D_t^{\alpha,0} f)(t) = \frac{1}{\Gamma(n-\alpha)} \int_0^t (t-\tau)^{n-\alpha-1} \frac{d^n f(\tau)}{d\tau^n}\, d\tau.$$

Definition 2.4. ([29]) Laplace transform of fractional operators. For order $\alpha > 0$, the Laplace transform of the fractional derivative is

$$\mathcal{L}\{D^\alpha f(t)\}(s) = s^\alpha \mathcal{L}\{f(t)\}(s) - \sum_{k=0}^{m-1} s^{\alpha-k-1} f^{(k)}(0),$$

where $m = \lceil \alpha \rceil$. For the fractional integral,

$$\mathcal{L}\{J^\alpha f(t)\}(s) = \frac{\mathcal{L}\{f(t)\}(s)}{s^\alpha}.$$

These relations simplify fractional equations into algebraic form in the s-domain.

Definition 2.5. ([28]) Mittag–Leffler function. The Mittag–Leffler function is

$$E_{\alpha,\beta}(z) = \sum_{n=0}^{\infty} \frac{z^n}{\Gamma(\alpha n + \beta)},$$

with parameters α, β. Its inverse $E^{-1}_{\alpha,\beta}(w)$ is usually computed numerically.

Theorem 2.1. *For a sufficiently smooth function $f(t)$, the Laplace transform of the tempered Caputo derivative satisfies*

$$\mathcal{L}\left\{{}^{C}D_t^{\alpha,\theta} f(t)\right\}(s) = (s+\theta)^{\alpha}\hat{f}(s) - (s+\theta)^{\alpha-1} f(0),$$

where $\hat{f}(s) = \mathcal{L}\{f(t)\}(s)$.

Proof. By definition, the tempered Caputo derivative is

$${}^{C}D_t^{\alpha,\theta} f(t) = \frac{1}{\Gamma(1-\alpha)} \int_0^t (t-\tau)^{-\alpha} e^{-\theta(t-\tau)} f'(\tau)\, d\tau.$$

Taking the Laplace transform of both sides gives

$$\mathcal{L}\left\{{}^{C}D_t^{\alpha,\theta} f(t)\right\}(s) = \int_0^{\infty} e^{-st} \left[\frac{1}{\Gamma(1-\alpha)} \int_0^t (t-\tau)^{-\alpha} e^{-\theta(t-\tau)} f'(\tau)\, d\tau\right] dt.$$

Switching the order of integration using Fubini's theorem:

$$\mathcal{L}\left\{{}^{C}D_t^{\alpha,\theta} f(t)\right\}(s) = \frac{1}{\Gamma(1-\alpha)} \int_0^{\infty} f'(\tau) \left[\int_{\tau}^{\infty} (t-\tau)^{-\alpha} e^{-(s+\theta)(t-\tau)}\, dt\right] d\tau.$$

Let $u = t - \tau \Rightarrow du = dt$. Then:

$$\int_{\tau}^{\infty} (t-\tau)^{-\alpha} e^{-(s+\theta)(t-\tau)}\, dt = \int_0^{\infty} u^{-\alpha} e^{-(s+\theta)u}\, du = \Gamma(1-\alpha)(s+\theta)^{\alpha-1}.$$

Substituting this result:

$$\mathcal{L}\left\{{}^{C}D_t^{\alpha,\theta} f(t)\right\}(s) = (s+\theta)^{\alpha-1} \int_0^{\infty} f'(\tau) e^{-s\tau}\, d\tau.$$

Using the Laplace transform property $\mathcal{L}\{f'(t)\} = s\hat{f}(s) - f(0)$, we obtain:

$$\mathcal{L}\left\{{}^{C}D_t^{\alpha,\theta} f(t)\right\}(s) = (s+\theta)^{\alpha}\hat{f}(s) - (s+\theta)^{\alpha-1} f(0). \tag{2.4}$$

Hence, we have established Theorem 2.1, showing that tempering (θ) modifies the standard fractional derivative in the Laplace domain. □

Lemma 2.1. *Consider the rectangular domain $\Omega = [0, L_x] \times [0, L_y]$. The set of functions*

$$\varphi_{m,n}(x,y) = \sin\left(\frac{m\pi x}{L_x}\right) \sin\left(\frac{n\pi y}{L_y}\right), \qquad m, n \in \mathbb{N},$$

constitutes an orthogonal and complete system in $L^2(\Omega)$. Consequently, any square-integrable initial distribution $f(x,y) \in L^2(\Omega)$ can be expressed uniquely as a Fourier sine series in terms of $\{\varphi_{m,n}\}$ [15].

Theorem 2.2 (Analytical solution of tempered time-fractional AD equation)**.** *Let* $\Omega = [0, L_x] \times [0, L_y]$ *and consider*

$$ {}^{C}D_t^{\alpha,\theta} C = D(C_{xx} + C_{yy}) - u_x C_x - u_y C_y, \quad C|_{\partial\Omega} = 0, \quad C(x, y, 0) = f(x, y) \in L^2(\Omega), $$

with $0 < \alpha \leq 1$, $\theta \geq 0$, $D > 0$, $u_x, u_y \in \mathbb{R}$.

Then, the unique solution is

$$ C(x, y, t) = \sum_{n,m=1}^{\infty} A_{n,m} \sin \frac{n\pi x}{L_x} \sin \frac{m\pi y}{L_y} \, e^{-\theta t} E_{\alpha,1}(-\lambda_{n,m} t^{\alpha}), $$

where $\lambda_{n,m} = D(n^2\pi^2/L_x^2 + m^2\pi^2/L_y^2)$ *and* $A_{n,m}$ *are the Fourier sine coefficients of* $f(x, y)$.

Proof. The scalar concentration field $C(x, y, t)$ can be represented using the separation of variables technique. This procedure leads to an infinite series expansion expressed in terms of orthogonal eigenfunctions. The structure of these eigenfunctions, denoted by $\varphi_{m,n}(x, y)$, is dictated by the requirement to satisfy homogeneous boundary conditions along the boundary of the domain. For a rectangular region $\Omega = [0, L_x] \times [0, L_y]$ subject to Dirichlet conditions ($C = 0$ on $\partial\Omega$), the admissible eigenfunctions naturally take the form of a sine series basis. The admissible eigenfunctions satisfying the homogeneous Dirichlet boundary conditions on the rectangle $\Omega = [0, L_x] \times [0, L_y]$ are given by

$$ \varphi_{m,n}(x, y) = \sin\left(\frac{m\pi x}{L_x}\right) \sin\left(\frac{n\pi y}{L_y}\right), \qquad m, n = 1, 2, 3, \ldots $$

The complete solution can, therefore, be expressed as a linear combination of these spatial modes, each weighted by a time-dependent amplitude:

$$ C(x, y, t) = \sum_{m=1}^{\infty} \sum_{n=1}^{\infty} T_{n,m}(t) \, \varphi_{m,n}(x, y). \tag{2.5} $$

The functions $T_{n,m}(t)$ are obtained by substituting the series expansion into the governing equation. The initial condition $C(x, y, 0) = f(x, y)$ is then applied to determine the constants, which fix the coefficients of the eigenfunctions in the solution. Now equation (1.1) reduces to

$$ \begin{aligned} \sum_{n=1}^{\infty} \sum_{m=1}^{\infty} T_{n,m}(t) \, \phi_n(x)\psi_m(y) = D\nabla^2 &\left(\sum_{n=1}^{\infty} \sum_{m=1}^{\infty} T_{n,m}(t) \, \phi_n(x)\psi_m(y) \right) \\ &- u_x \frac{\partial}{\partial x} \left(\sum_{n=1}^{\infty} \sum_{m=1}^{\infty} T_{n,m}(t) \, \phi_n(x)\psi_m(y) \right) \\ &- u_y \frac{\partial}{\partial y} \left(\sum_{n=1}^{\infty} \sum_{m=1}^{\infty} T_{n,m}(t) \, \phi_n(x)\psi_m(y) \right). \end{aligned} $$

The functions are defined as $\phi_n(x) = \sin\left(\frac{n\pi x}{L_x}\right)$, $\psi_m(y) = \sin\left(\frac{m\pi y}{L_y}\right)$, where L_x and L_y are the lengths of the domain in the x- and y-directions, respectively. □

Using the linearity of the operators, we obtain the following.

$$ \sum_{n=1}^{\infty} \sum_{m=1}^{\infty} T_{n,m}(t) \, \phi_n(x)\psi_m(y) = \sum_{n=1}^{\infty} \sum_{m=1}^{\infty} T_{n,m}(t) \Big[D\big(\phi_n''(x)\psi_m(y) + \phi_n(x)\psi_m''(y)\big) $$

$$- u_x\,\phi_n'(x)\psi_m(y) - u_y\,\phi_n(x)\psi_m'(y)\Big].$$

We now project into a specific mode by multiplying both sides of the equation with $\phi_k(x)\psi_l(y)$ and integrating over the domain Ω:

$$\begin{aligned}&\int_0^{L_y}\int_0^{L_x}\left(\sum_{n=1}^{\infty}\sum_{m=1}^{\infty}T_{n,m}(t)\,\phi_n(x)\psi_m(y)\right)\phi_k(x)\psi_l(y)\,dx\,dy\\ &=\int_0^{L_y}\int_0^{L_x}\left(\sum_{n=1}^{\infty}\sum_{m=1}^{\infty}T_{n,m}(t)\Big[D\big(\phi_n''(x)\psi_m(y)+\phi_n(x)\psi_m''(y)\big)\right.\\ &\quad\left.-u_x\,\phi_n'(x)\psi_m(y)-u_y\,\phi_n(x)\psi_m'(y)\Big]\right)\phi_k(x)\psi_l(y)\,dx\,dy.\end{aligned}$$

By orthogonality, all terms vanish except when $n=k$ and $m=l$:

$$\text{LHS} = T_{k,l}(t)\int_0^{L_x}\phi_k^2(x)\,dx\int_0^{L_y}\psi_l^2(y)\,dy\ = T_{k,l}(t)\frac{L_x}{2}\frac{L_y}{2}.$$

We analyze the four terms on the RHS separately:

Dispersion Term 1 ($D\,\phi_n''\psi_m$):

$$D\sum_{n,m}T_{n,m}(t)\int_0^{L_x}\phi_n''(x)\phi_k(x)\,dx\int_0^{L_y}\psi_m(y)\psi_l(y)\,dy.$$

Since $\phi_n''(x) = -\lambda_n^{(x)}\phi_n(x)$, with $\lambda_n^{(x)} = \left(\frac{n\pi}{L_x}\right)^2$, and $\int_0^{L_y}\psi_m(y)\psi_l(y)\,dy = \frac{L_y}{2}\,\delta_{m,l}$,

$$-D\lambda_k^{(x)}T_{k,l}(t)\frac{L_y}{2}\int_0^{L_x}\phi_k^2(x)\,dx = -D\lambda_k^{(x)}T_{k,l}(t)\frac{L_y}{2}\frac{L_x}{2}.$$

Dispersion Term 2 ($D\,\phi_n\psi_m''$): By the same reasoning, we get

$$-D\lambda_l^{(y)}T_{k,l}(t)\frac{L_x}{2}\frac{L_y}{2},\qquad \lambda_l^{(y)} = \left(\tfrac{l\pi}{L_y}\right)^2.$$

Advection Terms ($-u_x\phi_n'\psi_m,\ -u_y\phi_n\psi_m'$): For the sine basis with homogeneous Dirichlet boundary conditions, $\phi_n(0)=\phi_n(L_x)=0$ and $\psi_m(0)=\psi_m(L_y)=0$.

Define

$$I_{n,k}^{(x)} = \int_0^{L_x}\phi_n'(x)\phi_k(x)\,dx.$$

Integration by parts gives

$$I_{n,k}^{(x)} = \Big[\phi_n(x)\phi_k(x)\Big]_0^{L_x} - \int_0^{L_x}\phi_n(x)\phi_k'(x)\,dx = 0 - I_{k,n}^{(x)}.$$

Thus, $I_{k,n}^{(x)} = -I_{n,k}^{(x)}$, implying $2I_{n,k}^{(x)} = 0$, so $I_{n,k}^{(x)} = 0$ for all n,k. If the advection velocity is uniform, the projection removes the advection terms. When the velocity varies, the modes are no longer independent, and the solution needs to be modified.

Similarly, for

$$I_{m,l}^{(y)} = \int_0^{L_y}\psi_m'(y)\psi_l(y)\,dy,$$

we also obtain $I^{(y)}_{m,l} = 0$. Therefore, the Galerkin projections of the advection terms vanish:

$$\int_\Omega (\phi_n'(x)\psi_m(y))(\phi_k(x)\psi_l(y))\,dx\,dy = I^{(x)}_{n,k}\int_0^{L_y}\psi_m(y)\psi_l(y)\,dy = 0,$$
$$\int_\Omega (\phi_n(x)\psi_m'(y))(\phi_k(x)\psi_l(y))\,dx\,dy = \left(\int_0^{L_x}\phi_n(x)\phi_k(x)\,dx\right) I^{(y)}_{m,l} = 0.$$

Thus, the advection contributions vanish in every modal equation. Finally, canceling the common factor $\frac{L_xL_y}{4}$ from both sides, we obtain the governing equation for each mode (n, m).

$$ {}^{C}D_t^{\alpha,\theta}T_{n,m}(t) + \lambda_{n,m}\,T_{n,m}(t) = 0, \tag{2.6}$$

where the eigenvalue $\lambda_{n,m}$ combines the contributions from both spatial directions:

$$\lambda_{n,m} = D\left(\lambda_n^{(x)} + \lambda_m^{(y)}\right) = D\left(\frac{n^2\pi^2}{L_x^2} + \frac{m^2\pi^2}{L_y^2}\right).$$

The initial condition for each mode is given by

$$T_{n,m}(0) = A_{n,m}.$$

We now solve the corresponding initial value problem for the modal amplitude:

$$ {}^{C}D_t^{\alpha,\theta}T(t) + \lambda\,T(t) = 0, \qquad T(0) = A. \tag{2.7}$$

From the equation (2.4)

$$\mathcal{L}\left\{{}^{C}D_t^{\alpha,\theta}T(t)\right\}(s) = (s+\theta)^\alpha\,\hat{T}(s) - (s+\theta)^{\alpha-1}T(0),$$

where $\hat{T}(s)$ represents the Laplace transform of $T(t)$. From the general expression in equation (2.7),

$$(s+\theta)^\alpha\,\hat{T}(s) - (s+\theta)^{\alpha-1}T(0) + \lambda\,\hat{T}(s) = 0.$$

Solving for $\hat{T}(s)$, we obtain

$$\left[(s+\theta)^\alpha + \lambda\right]\hat{T}(s) = (s+\theta)^{\alpha-1}A, \tag{2.8}$$

which gives

$$\hat{T}(s) = A\,\frac{(s+\theta)^{\alpha-1}}{(s+\theta)^\alpha + \lambda}. \tag{2.9}$$

The expression in equation (2.9) is of standard form and its inverse Laplace transform

$$\mathcal{L}^{-1}\left\{\frac{(s+\theta)^{\alpha-1}}{(s+\theta)^\alpha + \lambda}\right\}(t) = e^{-\theta t}\,E_{\alpha,1}(-\lambda t^\alpha), \tag{2.10}$$

where $E_{\alpha,\beta}(z)$ is the two-parameter Mittag–Leffler function. Therefore, the solution to the modal problem (2.6) is

$$T_{n,m}(t) = A_{n,m}\,e^{-\theta t}\,E_{\alpha,1}(-\lambda_{n,m}t^\alpha). \tag{2.11}$$

Substituting the modal solution (2.6) back into the series expansion (2.5), we arrive at the final solution

$$C(x,y,t) = \sum_{n=1}^{\infty}\sum_{m=1}^{\infty} A_{n,m}\,\sin\!\left(\frac{n\pi x}{L_x}\right)\sin\!\left(\frac{m\pi y}{L_y}\right) \times e^{-\theta t}\,E_{\alpha,1}\!\left(-D\left(\frac{n^2\pi^2}{L_x^2}+\frac{m^2\pi^2}{L_y^2}\right)t^{\alpha}\right). \tag{2.12}$$

The coefficients $A_{n,m}$ are obtained from the initial condition by

$$A_{n,m} = \frac{4}{L_x L_y}\int_0^{L_y}\int_0^{L_x} f(x,y)\,\sin\!\left(\frac{n\pi x}{L_x}\right)\sin\!\left(\frac{m\pi y}{L_y}\right)\,dx\,dy. \tag{2.13}$$

The analytical solution of the tempered time-fractional advection–diffusion equation is derived in this study. While the focus is on obtaining the analytical formulation, theoretical aspects concerning existence, uniqueness, and convergence can be established similar to previous studies. For instance, Zaky (2019) [40] rigorously analyzed tempered fractional boundary value problems and proved the existence, uniqueness, and stability of solutions. Likewise, Obeidat et al. (2026) [26] provided comprehensive proofs addressing existence, uniqueness, and error estimates for nonlinear time-fractional diffusion equations. Following these works, analogous theoretical results can be derived for the present model, reinforcing the reliability of the obtained solution.

2.1. Model consistency and limiting behavior

No tempering ($\theta = 0$)

When $\theta = 0$, the tempered Caputo derivative simplifies to the classical Caputo operator (${}^{C}D_t^{\alpha}$). In this case, the solution reduces to

$$C(x,y,t) = \sum_{n=1}^{\infty}\sum_{m=1}^{\infty} A_{n,m}\,\phi_n(x)\psi_m(y)\,E_{\alpha,1}(-\lambda_{n,m}t^{\alpha}).$$

This represents the standard form of the time-fractional diffusion equation in the absence of tempering.

Classical diffusion limit ($\alpha \to 1$)

The Mittag–Leffler function satisfies the identity $E_{1,1}(z) = e^{z}$. Hence,

$$\lim_{\alpha\to 1} C(x,y,t) = \sum_{n=1}^{\infty}\sum_{m=1}^{\infty} A_{n,m}\,\phi_n(x)\psi_m(y)\,e^{-\theta t}\,e^{-\lambda_{n,m}t},$$

which can be written as

$$\sum_{n=1}^{\infty}\sum_{m=1}^{\infty} A_{n,m}\,\phi_n(x)\psi_m(y)\,e^{-(\lambda_{n,m}+\theta)t}.$$

This corresponds to the classical diffusion equation with an additional linear sink term $-\theta C$. The presence of the tempering parameter θ accelerates the exponential decay of each mode.

Physical interpretation of θ

The multiplicative term $e^{-\theta t}$ modulates the entire solution. In the case of fractional diffusion with $\alpha < 1$, the Mittag–Leffler function exhibits algebraic (power-law) decay at large times, producing long memory and heavy-tail effects. The tempering factor $e^{-\theta t}$ overrides this slow decay at long times, enforcing an exponential cutoff while still retaining the anomalous, non-Markovian characteristics at short and intermediate time scales. As a result, the tempered model provides a more realistic representation of many physical and environmental processes.

3. Analytical results and discussion

3.1. Effect of α and θ on $C(x,t)$ at $t = 0.8$ ($D = 0.1$)

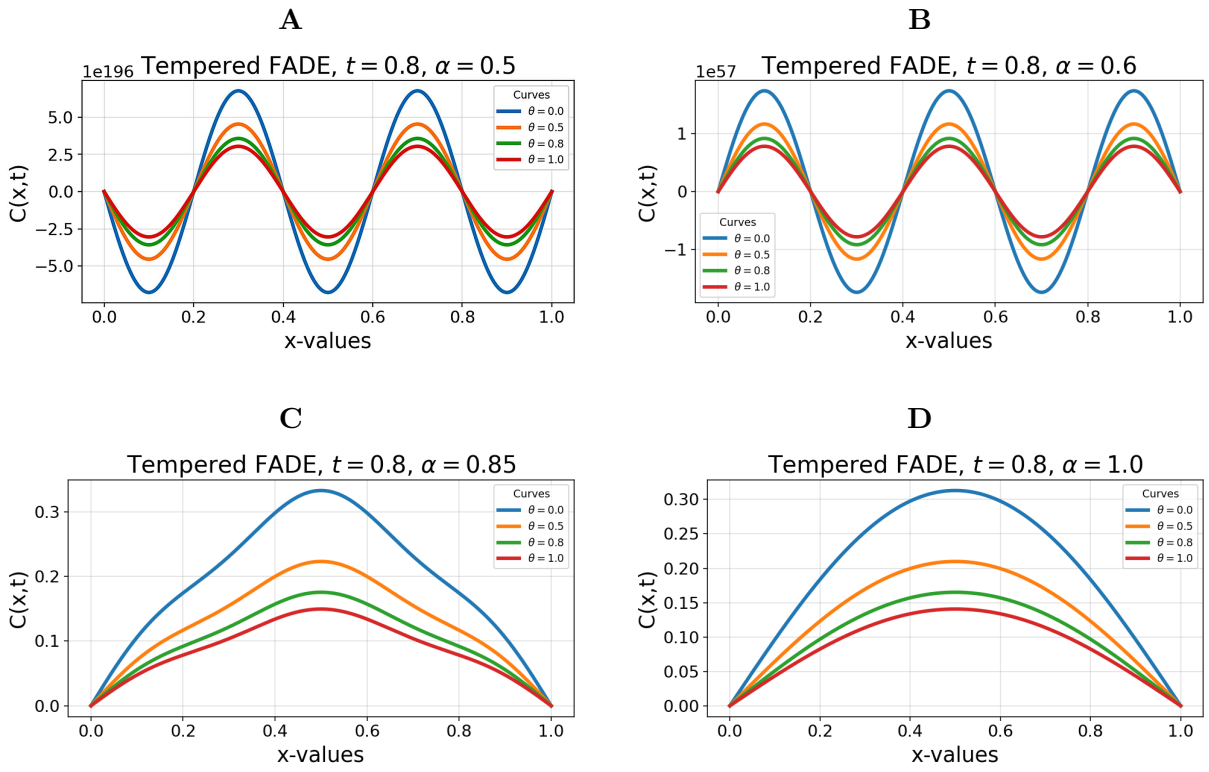

Figure 1. At $t = 0.8$ with $D = 0.1$, $L = 1$ (Dirichlet; Gaussian–sine $f(x)$). Each panel shows $\theta \in \{0, 0.5, 0.8, 1.0\}$. A: $\alpha = 0.5$: slow decay, broad plume. B: $\alpha = 0.6$: faster yet subdiffusive. C: $\alpha = 0.85$: near-classical, smoother. D: $\alpha = 1.0$: classical, lowest/most compact. Larger θ lowers peaks and narrows spread.

Figure 1. Impact of fractional order and tempering at $t = 0.8$, $D = 0.1$. A: $\alpha = 0.5$ (subdiffusion). The presence of strong memory effects decelerates the decay, resulting in a broad profile with a relatively high peak. Increasing $\theta \in [0, 1]$ (via $e^{-\theta t}$) monotonically reduces the peak and narrows the plume, thereby suppressing long-time tails. B: $\alpha = 0.6$ (moderate subdiffusion). The decay rate is faster than at $\alpha = 0.5$, yet memory effects still maintain a broader plume compared to near-classical behavior. A larger θ monotonically decreases both amplitude and spread; higher spatial modes are damped earlier, yielding a smoother and more localized curve. C: $\alpha = 0.85$ (near-classical). The plume is overall smoother and lower, with most high-frequency

content dissipated by $t = 0.8$. Tempering primarily reduces the tail; a larger θ further compresses the distribution, driving it toward an exponential-like clearance. D: $\alpha = 1.0$ (classical diffusion). Each sine mode decays as $e^{-(\lambda_n+\theta)t}$, resulting in the lowest and most compact profile among the four α values. Increasing θ uniformly accelerates exponential damping (a linear sink); Dirichlet endpoints remain zero, and the shape is dominated by the lowest modes.

For any given α, an increase in θ results in a reduction of the peak of $C(x,t)$ and a narrowing of the plume, which aligns with an exponential cut-off point of memory. When θ is held constant, a decrease in α enhances memory, leading to higher and broader profiles; the observed order by amplitude is $\alpha = 0.5 > 0.6 > 0.85 > 1.0$. The effect of tempering is most pronounced at lower values of α (e.g., $\alpha = 0.5$), whereas α approaches 1, the response converges towards classical diffusion, with θ functioning as a uniform sink.

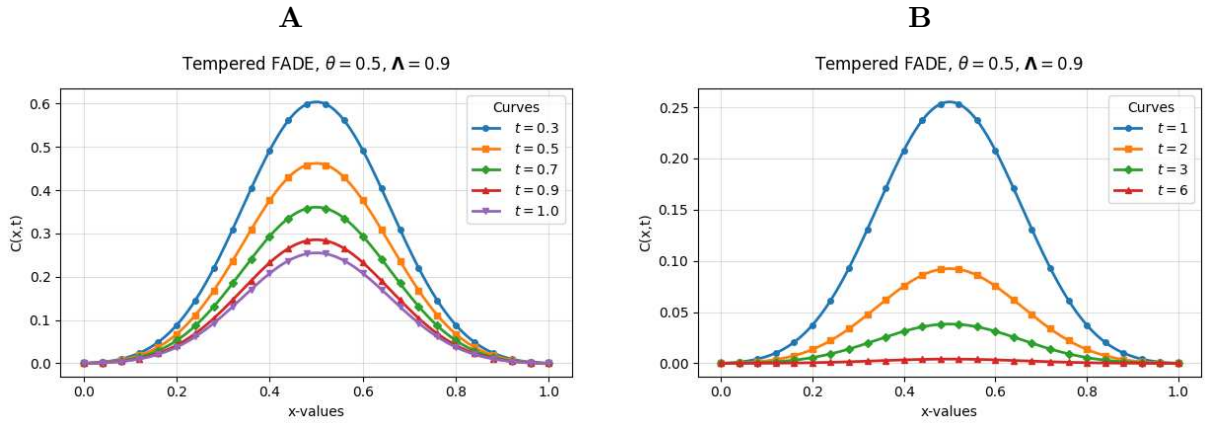

Figure 2. Temporal evolution of 1D tempered FADE ($D = 0.1$, $\alpha = 0.8$, $\theta = 0.5$, $\lambda = 0.9$) from a Gaussian–sine initial state. A: Short times (t = 0.3–1.0) show rapid decay and subdiffusive spreading, B: While longer times (t = 1-6) reveal strong tempering-induced damping and dispersion.

3.1.1. Early-and intermediate-time evolution

Figure 2 A: $C(x,t)$ decays monotonically while retaining the initial Gaussian–sine shape: At $t = 0.3$ the peak near $x = 0.5$ is still high ($C_{\max} \approx 0.85$) with little spreading; by $t = 0.5$ decay and mild broadening appear ($C_{\max} \approx 0.68$); at $t = 0.7$ smoothing intensifies ($C_{\max} \approx 0.54$); by $t = 0.9$ and 1.0, attenuation is marked ($C_{\max} \approx 0.43$ and 0.38), totaling $\sim$ 55% drop from the start. Dirichlet endpoints remain zero. Figure 2 B: Exponential tempering dominates: From $t = 1$ to $t = 2$, $C_{\max}$ drops to ≈ 0.14 (additional $\sim$ 63% drop; consistent with $e^{-\theta t}$, $\theta = 0.5 \Rightarrow e^{-1}$). At $t = 3$, $C_{\max} \approx 0.05$ and the profile is nearly homogeneous; by $t = 4$, $C_{\max} \approx 0.02$ and the curve is essentially flat, contrasting with the slower power-law decay of untempered fractional diffusion. Figure 2 shows that $C(x,t)$ decays rapidly: Short times (t = 0.3–1.0) preserve the Gaussian–sine shape with $\sim$ 55% peak reduction, while medium times (t = 1–4) exhibit strong tempering, driving the profile toward near-flatness in contrast to untempered fractional diffusion.

3.2. Visualizing tempering effects in two-dimensional fractional diffusion

Table 2 lists the center-point concentration $C(0.5, 0.5, t)$ from the 2-D tempered fractional advection–diffusion model, with rows as selected times and columns as tempering levels θ.

Table 2. Concentration $C(t, \theta)$ for selected t and θ.

t	$\theta = 0.0$	$\theta = 0.1$	$\theta = 0.5$	$\theta = 0.7$	$\theta = 0.9$	$\theta = 1.0$
0.0	9.999×10^{-1}	9.999×10^{-1}	9.999×10^{-1}	9.999×10^{-1}	9.999×10^{-1}	9.999×10^{-1}
0.2	9.321×10^{56}	9.136×10^{56}	8.434×10^{56}	8.103×10^{56}	7.785×10^{56}	7.631×10^{56}
0.5	7.315×10^{59}	6.958×10^{59}	5.697×10^{59}	5.155×10^{59}	4.664×10^{59}	4.437×10^{59}
0.7	4.993×10^{52}	4.655×10^{52}	3.518×10^{52}	3.059×10^{52}	2.659×10^{52}	2.479×10^{52}
1.0	6.536×10^{44}	5.914×10^{44}	3.964×10^{44}	3.245×10^{44}	2.657×10^{44}	2.404×10^{44}

At $t = 0$ all entries coincide, since tempering acts only through time. For any fixed $t > 0$, values decrease monotonically with θ due to the uniform damping $\exp(-\theta t)$. Relative to the untempered baseline $C_0 = C|_{\theta=0}$, the ratios for $\theta = 1$ are $C/C_0 \approx 0.82$ at $t = 0.2$, 0.61 at $t = 0.5$, and 0.37 at $t = 1.0$. Down each column (fixed θ), concentrations decline with t under $\exp(-\theta t)E_{\alpha,1}(-\lambda t^\alpha)$. Although magnitudes depend on D, α, mode truncation, and the initial condition, the qualitative pattern—identical start, stronger damping for larger θ, and overall decay over time—remains the same.

Figure 3 ($A_{\theta=0.0}$, $B_{\theta=0.5}$, $C_{\theta=1.0}$). At $t = 0.2$ with diffusion $D = 0.1$ (so $\lambda_{11} = 2D\pi^2 = 0.2\pi^2$), the fields $C(x, y, t)$ on $[0, 1]^2$ all display the same single-hump pattern $\sin(\pi x)\sin(\pi y)$: The values vanish on $\partial\Omega$ and attain a unique maximum at $(0.5, 0.5)$. The tempering parameter θ appears only in the temporal factor $\exp(-\theta t)E_{\alpha,1}(-\lambda_{11} t^\alpha)$; hence larger θ uniformly reduces the magnitude while leaving the geometry unchanged, yielding the peak ordering $A_{\theta=0.0} > B_{\theta=0.5} > C_{\theta=1.0}$. A common color scale at this time level makes this uniform reduction evident. The fractional index α controls the short-time deviation from the initial state through the Mittag-Leffler term, whereas θ acts as a domain-wide clearance rate; together they separate a fixed spatial shape (set by the eigenfunction) from an amplitude governed by tempering.

4. Application to pollutant dispersion in urban street canyons

The model in this work is well suited to predict how pollution spreads inside urban street canyons narrow roads bordered by tall buildings. In these spaces, the air moves in complex patterns, such as recirculating eddies and along-street channeling, so basic diffusion models often fail to match what we observe. The tempered fractional approach keeps short-term memory effects while preventing unrealistically long persistence, making the predictions more realistic for confined street-canyon settings.

Physical context

Urban street canyons exhibit distinctive physical characteristics that influence pollutant behavior. The presence of tall buildings limits vertical airflow, leading to the accumulation of pollutants. Air movement within these canyons is often turbulent and complex, causing deviations from standard diffusion patterns. Due to weak ventilation and intricate flow structures, pollutants can persist for extended periods; however, they are gradually removed through restricted diffusion and intermittent horizontal airflows, which limit their residence time within the canyon.

Model Parameterization: In a typical urban street canyon, the characteristic length scales and

flow parameters are defined as follows: The street width is generally approximately $L_x = 20\,\mathrm{m}$, while the average building height is around $L_y = 30\,\mathrm{m}$. The effective eddy diffusivity, which represents turbulent mixing, typically ranges from $D = 0.1$–$1.0\,\mathrm{m}^2/\mathrm{s}$. Wind velocity along the street axis is relatively higher, with values between $u_x = 0.5$–$2.0\,\mathrm{m/s}$, whereas cross-street ventilation is weaker, ranging from $u_y = 0.1$–$0.5\,\mathrm{m/s}$. These parameter selections reflect the confined geometry of canyons, where pollutant transport is influenced by limited mixing and directional airflows.

The fractional exponent $\alpha \in (0.6, 0.9)$ is indicative of subdiffusive transport, which reflects

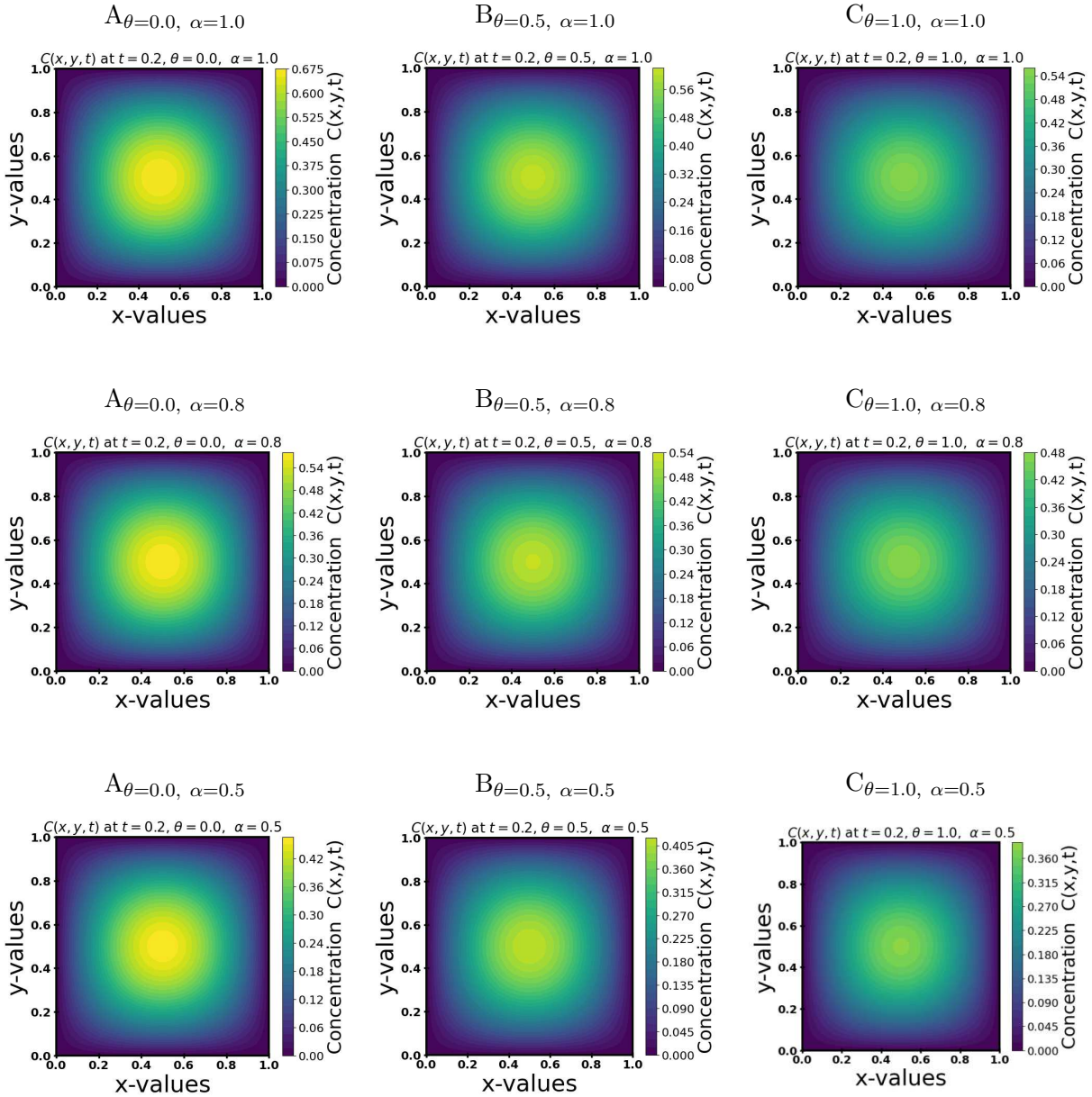

Figure 3. Temporal evolution of 1D tempered FADE ($D = 0.1$, $\alpha = 0.8$, $\theta = 0.5$, $\lambda = 0.9$) from a Gaussian–sine initial state. A: Short times ($t = 0.3$–1.0) show rapid decay and subdiffusive spreading, B: While longer times ($t = 1$-6) reveal strong tempering-induced damping and dispersion.

the impact of turbulence and recirculating flows induced by building structures. The tempering coefficient $\theta \in (0.1, 0.5)\,\mathrm{s}^{-1}$ represents the effective rate of pollutant removal, taking into account limited ventilation and surface deposition. In urban canyon environments, selecting α within the range of 0.6 to 0.9 signifies the subdiffusive transport resulting from turbulence and recirculation, while setting θ between 0.1 and $0.5\,\mathrm{s}^{-1}$ denotes pollutant clearance through weak ventilation and surface deposition. These values correspond with timescales observed in field studies of street-canyon dispersion.

Case study: Traffic-related emissions

We investigate the dispersion of pollutants emitted from vehicles, where the initial concentration is described by

$$f(x, y) = C_0 \exp\left(-\frac{(x - x_0)^2}{2\sigma_x^2} - \frac{(y - y_0)^2}{2\sigma_y^2}\right),$$

with (x_0, y_0) representing the source location and σ_x, σ_y defining the initial spread of the emission plume. The model reveals three distinct temporal phases. In the early stage ($t < 1\,\mathrm{h}$), the system behavior is largely dictated by the fractional order α, resulting in subdiffusive transport that slows the plume's spread relative to classical diffusion and maintains higher concentrations near the source. During the intermediate stage ($1 \leq t \leq 4\,\mathrm{h}$), both memory effects and the tempering parameter θ influence dispersion, producing transitional dynamics that bridge anomalous retention and gradual decay. In the late stage ($t > 4\,\mathrm{h}$), the effect of θ predominates, inducing exponential attenuation that facilitates realistic pollutant removal, unlike untempered fractional models which tend to overestimate pollutant persistence.

Practical implications

The tempered fractional advection–diffusion framework provides multiple benefits for modeling urban pollutant dynamics by explicitly coupling anomalous dispersion with memory effects (α) and finite-range interactions (θ), which constitutes its core novelty. This enables more accurate evaluation of exposure by capturing both peak concentrations and the temporal evolution of pollutant plumes. Additionally, it supports effective mitigation strategies and urban planning applications by highlighting how the layout and structure of urban environments influence the retention and removal of pollutants. It also provides quantitative guidance for regulatory and policy decisions by producing realistic decay rates and risk assessments that align with environmental standards. This case study demonstrates that the proposed framework successfully represents complex urban transport phenomena, including both anomalous dispersion and finite-time clearance, reflecting the combined effects of fractional memory and tempering. These results offer actionable insights for air quality management, emergency response, and decision-making in urban environments.

As illustrated in Figure 4, the evolution of the pollutant plume is analyzed under varying fractional orders and temporal conditions, with dimensions $L_x = 20\,\mathrm{m}$ and $L_y = 30\,\mathrm{m}$. The process is modeled using the tempered fractional advection–diffusion framework, characterized by a diffusion coefficient $D = 0.5\,\mathrm{m}^2/\mathrm{s}$, wind velocities $u_x = 1.0\,\mathrm{m/s}$, $u_y = 0.2\,\mathrm{m/s}$, and a tempering parameter $\theta = 0.1$. A series of surface and wireframe visualizations are utilized to investigate the evolution of pollutant concentration for fractional orders such as $\alpha = 0.8$ at specific time intervals. The surface plots depict the intensity and spatial distribution through

A: 3D Surface Plot
$\alpha = 0.8,\ \theta = 0.1,\ T = 1\,\mathrm{s}$

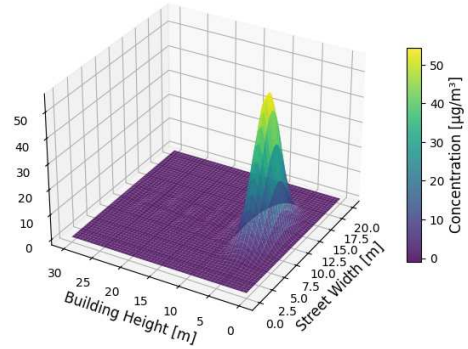

B: 3D Wireframe Plot
$\alpha = 0.8,\ \theta = 0.1,\ T = 1\,\mathrm{s}$

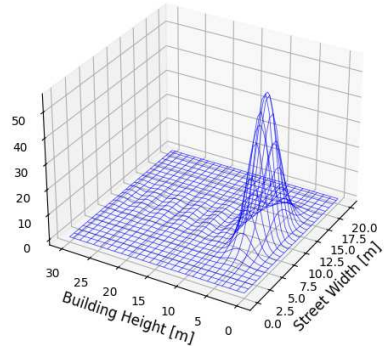

C: Surface Plot
$\alpha = 0.8,\ \theta = 0.1,\ T = 10\,\mathrm{s}$

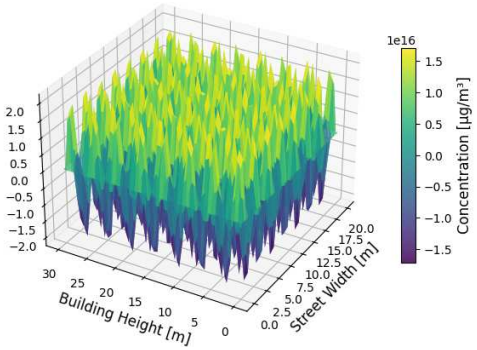

D: Wireframe Plot
$\alpha = 0.8,\ \theta = 0.1,\ T = 10\,\mathrm{s}$

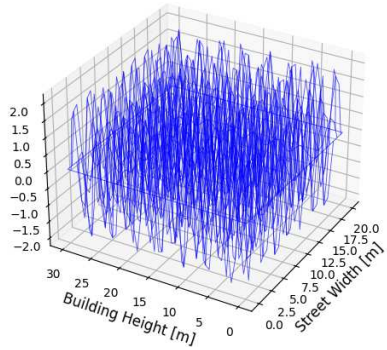

E: Surface Plot
$\alpha = 0.8,\ \theta = 0.1,\ T = 60\,\mathrm{s}$

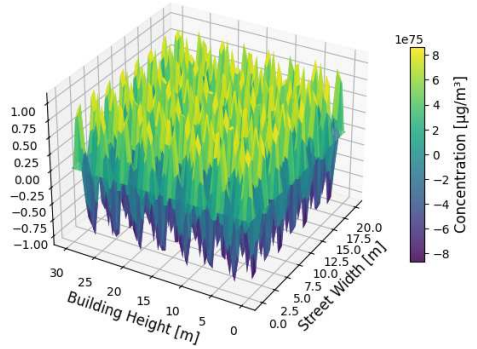

F: Wireframe Plot
$\alpha = 0.8,\ \theta = 0.1,\ T = 60\,\mathrm{s}$

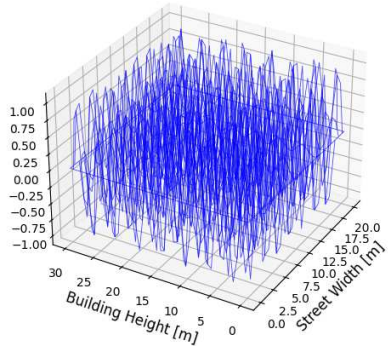

Figure 4. Three-dimensional pollutant dispersion in an urban street canyon ($L_x = 20\,\mathrm{m}$, $L_y = 30\,\mathrm{m}$, $D = 0.5\,\mathrm{m}^2/\mathrm{s}$, $u_x = 1.0\,\mathrm{m/s}$, $u_y = 0.2\,\mathrm{m/s}$, $\theta = 0.1$) modeled using the tempered fractional advection–diffusion equation. Surface plots (A, C, E) and wireframe plots (B, D, F) illustrate the influence of time on pollutant dispersion for fractional order $\alpha = 0.8$.

color shading and height variation, while the wireframe plots offer structural clarity of the dispersive field.

These results explicitly illustrate the physical phenomena of urban pollutant dispersion that can be described by the theoretical framework. For instance, subdiffusive transport (smaller α) corresponds to pollutant trapping in narrow street canyons or areas with limited ventilation, while larger α reflects faster dispersion akin to classical diffusion in more open urban spaces. The tempering parameter θ models the effect of finite-range interactions, such as the natural decay of pollutants or removal via ventilation, ensuring that long-tailed concentration profiles eventually clear, consistent with observed urban air quality data. The findings indicate that smaller values of α result in slower dispersion with broader plumes, whereas larger values exhibit behavior akin to classical diffusion. Overall, the model effectively captures the combined influence of fractional memory and exponential tempering in shaping pollutant transport within a confined urban geometry. By linking fractional parameters to physical transport regimes, the framework enables quantitative prediction of real urban phenomena, including pollutant accumulation near building facades, delayed plume clearance in low-wind areas, and the influence of street orientation on exposure hotspots.

The fractional order α dictates the transport regime: Smaller values produce slower, wider spreading patterns characteristic of subdiffusion, while larger values approach classical diffusion with more rapid decay and reduced peaks. The tempering parameter θ serves to attenuate long-range memory effects, thereby diminishing plume intensity. In the context of Kathmandu Valley, Nepal, observational evidence from Air Quality Index (AQI) monitoring stations provides experimental support for the physical transport mechanisms represented by the proposed model. Long-term measurements of $PM_{2.5}$, NO_x, and NH_3 consistently show concentration persistence, delayed decay, and strong diurnal variability, particularly under low-wind conditions and winter-time temperature inversions [29, 30]. These features indicate pollutant trapping within narrow street canyons and dense urban layouts, which corresponds to subdiffusive transport regimes characterized by smaller fractional orders α. Moreover, AQI time-series data frequently exhibit long-tailed decay after emissions subside, reflecting pronounced memory effects that are not adequately described by classical Gaussian diffusion models [38]. The eventual reduction of pollutant concentrations due to ventilation, chemical reactions, and atmospheric mixing is consistent with the finite-time clearance captured by the tempering parameter θ. Such behavior has been widely reported in Kathmandu, where $PM_{2.5}$ and NH_3 often remain elevated for extended periods, while NO_x shows relatively faster daytime decay driven by photochemical processes. These observations demonstrate that the tempered fractional advection–diffusion framework can realistically represent key urban transport phenomena, including pollutant accumulation near roadways, delayed plume dissipation under stagnant conditions, and spatially heterogeneous exposure hotspots. Consequently, the proposed model provides a physically grounded and practically relevant tool for urban air quality assessment and management in complex valley environments.

5. Conclusion

This study aimed to develop an analytical framework for addressing two-dimensional tempered time-fractional advection-diffusion equations within bounded domains. The findings reveal that an exact infinite-series solution can be obtained through eigenfunction expansion and Laplace transform techniques, articulated via sine spatial modes and a tempered Mittag-Leffler temporal

function. A key result is that the fractional order α dictates subdiffusive spreading and memory effects, while the tempering parameter θ governs exponential decay, enabling a clear distinction between spatial and temporal dispersion. This paper is the first to offer an exact solution for tempered fractional diffusion in a 2D confined domain, providing a valuable tool for modeling anomalous transport. A significant contribution is the model's ability to predict pollutant retention and clearance in urban street canyons with high physical fidelity. Practically, the model aids urban air quality management by accurately capturing pollutant dispersion and decay, thereby supporting risk assessment and mitigation strategies. Although limited to 2D domains and uniform parameters without explicit advection, this simplification allows for a fully analytical solution that isolates the effects of α and θ. Despite these limitations, the study significantly advances the understanding and modeling of anomalous transport. Future work could extend this framework to incorporate variable-order derivatives, complex boundaries, advection, and large-scale numerical simulations, as well as applications in porous media or biological systems. In summary, this work offers a rigorous, interpretable, and physically insightful model that bridges fractional calculus and practical environmental modeling, providing both theoretical and applied benefits for predicting pollutant dispersion in confined domains. The developed model serves as a theoretical benchmark for advancing fractional transport studies while simultaneously offering practical applicability in predicting pollutant dispersion within complex built environments.

CRediT authorship contribution statement

Shankar Pariyar: Conceptualization, methodological design, investigation, data analysis, data management, visualization, validation, Writing–original draft, and revision. **Bishnu P. Lamichhane:** Conceptualization, Methodology development, Visualization, Supervision, Validation, review and editing. **Jeevan Kafle:** Conceptualization, Methodology development, Validation, Visualization, Writing – review and editing. **Eeshwar P. Poudel:** Computational support and visualization.

References

[1] N. Akhtar, M. I. S. Ishak, S. A. Bhawani and K. Umar, *Various natural and anthropogenic factors responsible for water quality degradation*, Water, 2021, 13(19), 2660.

[2] R. Almeida, N. Martins and J. V. D. C. Sousa, *Fractional tempered differential equations*, AIMS Mathematics, 2024, 9(4), 9107–9127.

[3] L. Barsanti, L. Birindelli, A. Di Garbo and P. Gualtieri, *Bioconvection in microalgae*, Applied Sciences, 2025, 15(5), 2708.

[4] A. H. Bhrawy, A. S. Alofi and S. S. Ezz-Eldien, *Quadrature tau method for fractional equations*, Applied Mathematics Letters, 2011, 24(12), 2146–2152.

[5] A. H. Bhrawy and M. A. Zaky, *Jacobi tau approximation for fractional pdes*, Journal of Computational Physics, 2015, 281, 876–895.

[6] A. H. Bhrawy and M. A. Zaky, *Collocation methods for variable-order fractional Schrödinger equations*, Applied Numerical Mathematics, 2017, 111, 197–218.

[7] A. H. Bhrawy, M. A. Zaky and J. A. Tenreiro Machado, *Chebyshev tau approximation for fractional telegraph equations*, Journal of Optimization Theory and Applications, 2017, 174(1), 321–341.

[8] K. Ö. Çallı, G. Chiogna, D. Bittner and A. Hartmann, *Karst water resources in a changing world*, Reviews of Geophysics, 2025, 63(1), e2023RG000811.

[9] T. Cheng, J. Shao and Z. L. Wang, *Triboelectric nanogenerators*, Nature Reviews Methods Primers, 2023, 3(1), 39.

[10] A. G. Cherstvy, S. Thapa and R. Metzler, *Time averages for the Ornstein–Uhlenbeck process*, Physical Review E, 2018, 98(2), 022134.

[11] M. Dehghan and M. Abbaszadeh, *Element free Galerkin method for fractional cable equations*, Applied Numerical Mathematics, 2016, 109, 208–234.

[12] M. Dehghan, M. Abbaszadeh and W. Deng, *Fourth-order method for tempered diffusion-wave equations*, Applied Mathematics Letters, 2017, 73, 120–127.

[13] H. Ding and C. P. Li, *High-order algorithms for riesz derivatives*, Journal of Scientific Computing, 2017, 71(2), 759–784.

[14] H. Ding, C. P. Li and Y. Chen, *High-order algorithms for riesz derivatives (ii)*, Journal of Computational Physics, 2015, 293, 218–237.

[15] L. C. Evans, *Partial Differential Equations*, American Mathematical Society, Providence, 2010.

[16] C. Gerente, V. K. C. Lee, P. Le Cloirec and G. McKay, *Application of chitosan for the removal of metals from wastewaters by adsorption*, Critical Reviews in Environmental Science and Technology, 2007, 37(1), 41–127.

[17] F. S. Gittleson, R. E. Jones, D. K. Ward and M. E. Foster, *Oxygen solubility and transport in li–air battery electrolytes*, Energy & Environmental Science, 2017, 10(5), 1167–1179.

[18] Y. Hu, Q. Hu, H. Xue, et al., *Directional flow-induced non-fickian transport*, Physics of Fluids, 2025, 37(9), 096614.

[19] F. Hussain and M. ur Rehman, *On general tempered fractional calculus with luchko kernels*, Journal of Computational and Applied Mathematics, 2025, 458, 116339.

[20] N. Kumar and S. K. Basu, *Diffusive Processes and Modelling: An Introduction*, Springer, 2014.

[21] Y. Liang, W. Wang and R. Metzler, *Nonergodicity of confined fractional Brownian motion*, Physical Review E, 2023, 108(5), L052101.

[22] F. Liu, P. Zhuang, I. Turner, et al., *Adi method for fractional Fitzhugh–Nagumo systems*, Journal of Computational Physics, 2015, 293, 252–263.

[23] M. M. Meerschaert, F. Sabzikar and J. Chen, *Tempered fractional calculus*, Journal of Computational Physics, 2015, 293, 14–28.

[24] D. del Castillo-Negrete, *Fractional diffusion models of anomalous transport*, in *Anomalous Transport*, Wiley, 2008, 163–212.

[25] H. Niu, Y. Chen and B. J. West, *Fractional dynamics in big data and machine learning*, Entropy, 2021, 23(3), 297.

[26] N. A. Obeidat, M. E. Alkhamaiseh and M. S. Rawashdeh, *Using reliable techniques to solve nonlinear fractional differential equations along with theoretical analysis*, Journal of Applied Analysis & Computation, 2026, 16(1), 76–98.

[27] S. Pariyar and K. J., *An analytical framework for modeling urban pollutant dispersion with fractional transport dynamics*, Decision Analytics Journal, 2026, 100684.

[28] S. Pariyar and J. Kafle, *Fractional advection–diffusion equation with variable diffusivity: Pollutant effects using adomian decomposition method*, Applied Mathematics E-Notes, 2025, 25, 275–285.

[29] S. Pariyar, B. P. Lamichhane and J. Kafle, *A time fractional advection-diffusion approach to air pollution*, Partial Differential Equations in Applied Mathematics, 2025, 14, 101149.

[30] S. Pariyar, B. P. Lamichhane, J. Kafle and E. P. Poudel, *Three-dimensional time-fractional advection–diffusion modeling of pollutant dispersion: Analytical and numerical framework*, International Journal of Applied Mathematics, 2025, 38(12s).

[31] I. Podlubny, *Fractional Differential Equations*, Academic Press, 1999.

[32] A. Saadatmandi and M. Dehghan, *Operational matrix for fractional differential equations*, Computers & Mathematics with Applications, 2010, 59(3), 1326–1336.

[33] S. Sarker and O. T. Leta, *Review of watershed hydrology and mathematical models*, Engineering, 2025, 6(6), 129.

[34] R. Schumer, M. M. Meerschaert and B. Baeumer, *Fractional advection–dispersion equations for modeling transport at the earth surface*, Journal of Geophysical Research, 2009, 114, F00A07.

[35] F. Sultana, D. Singh, R. K. Pandey and D. Zeidan, *Numerical schemes for tempered fractional equations*, Applied Numerical Mathematics, 2020, 156, 74–95.

[36] M. Vellappandi and S. Lee, *Neural fractional differential networks*, Nonlinear Dynamics, 2025, 113(10), 12117–12130.

[37] W. Wang, A. G. Cherstvy, H. Kantz, et al., *Time averaging and emerging nonergodicity upon resetting*, Physical Review E, 2021, 104(2), 024105.

[38] W. Wang, R. Metzler and A. G. Cherstvy, *Anomalous diffusion, aging, and nonergodicity of scaled Brownian motion*, Physical Chemistry Chemical Physics, 2022, 24(31), 18482–18504.

[39] W. Wang, R. Metzler and I. M. Sokolov, *Restoring ergodicity of reset anomalous diffusion*, Physical Review Research, 2022, 4(1), 013161.

[40] M. A. Zaky, *Existence, uniqueness and numerical analysis of solutions of tempered fractional boundary value problems*, Applied Numerical Mathematics, 2019, 145, 429–457.

[41] M. Zayernouri and G. E. Karniadakis, *Fractional spectral collocation methods*, Journal of Computational Physics, 2015, 293, 312–338.

[42] Y. Zhang, X. Liu and H. Zhan, *Modeling hydrologically mediated hot moments of anomalous diffusion*, Water Resources Research, 2024, 60(3), e2023WR036089.

[43] X. Zhao, Z. Z. Sun and Z. P. Hao, *A fourth-order compact adi scheme for two-dimensional nonlinear space fractional Schrödinger equation*, SIAM Journal on Scientific Computing, 2014, 36(6), A2865–A2886.

Received October 2025; Accepted January 2026; Available online February 2026.